HiSST: 3rd International Conference on
High-Speed Vehicle Science Technology
14 -19 April 2024, Busan, Korea

Numerical investigation of magnetic heat flux and electron manipulation system for hypersonic vehicles

Thomas J. Greenslade[1], Arunkumar Chinnappan[2], and Minkwan Kim[3],

Abstract

The renewed interest in hypersonic flights has brought fresh attention to the physical challenges in reusable thermal protection systems. The need to enhance the reliability of hypersonic and re-entry vehicles has sharply focused on the limitations of our current comprehension of thermos-chemical non-equilibrium flows and our restricted predictive capabilities. This paper presents the work carried out by the University of Southampton and our consortium partners within the MEESST collaboration. This project is currently involved in both numerical and experimental research to develop magnetic shielding techniques for atmospheric re-entry vehicles. These techniques aim to offer additional approaches for mitigating heat flux. Here, we present the results of multi-physics simulations conducted with the University of Southampton's HANSA toolkit, along with comparisons, both experimental and numerical, produced by our consortium partners. These encompass simulations of multiple capsules undergoing atmospheric re-entry and simulations of ground-based experimental campaigns. We give particular attention to the effects of thermo-chemical non-equilibrium and MHD modeling. We illustrate the impacts of various mathematical models on the results obtained, with a strong emphasis on mission-critical parameters like surface heat fluxes and electron densities. We also present conclusions regarding the implications of these results on magnetic shielding designs. We demonstrate differences in thermal relaxation rates in terms of their effects on impinging heat fluxes. We then investigate the influence of these rate variations on magnetic heat flux mitigation techniques. Lastly, we offer an overview of current knowledge gaps in areas crucial to MEESST and lay out plans for future simulations and experiments, both within the MEESST project and beyond.

Keywords: *MEESST, MHD, TPS, HANSA, heatshield*

Nomenclature

B – Magnetic field
E_{ve} - vibrational-electronic energy
q_{tr} – translational and rotational heat flux
q_{tr}, q_{ve} and q_e are translational-rotational
τ - viscous stress tensor
E - total energy
E_e - electron energy
q_{tr} – vibrational and electronic heat flux
ρ_i - density of species Greek
δ_{ij} - Kronecker delta

1. Introduction

Returning to Earth after spaceflight presents a significant challenge, and there has been a notable resurgence of interest in both interplanetary and terrestrial spaceflight over the past decade. During atmospheric re-entry, the kinetic energy of a vehicle is converted into heat, raising the vehicle's surface temperature and ionising the surrounding air. This ionised air forms a thin and dense electron layer,

[1] *Post-doctoral Research Fellow, University of Southampton, University Road, Southampton, SO17 1BJ, UK, tg1u17@soton.ac.uk*
[2] *Post-doctoral Research Fellow, University of Southampton, University Road, Southampton, SO17 1BJ, UK, a.chinnappan@soton.ac.uk*
[3] *Associate Professor in Astronautics, University of Southampton, University Road, Southampton, SO17 1BJ, UK, m.k.kim@soton.ac.uk*

often referred to as a plasma sheath, around the vehicle. This plasma sheath effectively blocks the propagation of electromagnetic waves, resulting in what is commonly known as a radio or communication blackout. Although the radio blackout was initially observed during the early space race, it remains a challenge for capsule-shaped vehicles, both manned and unmanned.

The high thermal load experienced during atmospheric re-entry necessitates the use of a thermal protection system (TPS) to absorb and dissipate the substantial heating encountered. While both ablating and non-ablating TPS are available, non-ablating TPS is more commonly used because of its ability to withstand higher heat loads through the process of phase change and mass loss. Ablative TPS materials typically consist of carbon or silica fibres embedded within a phenolic resin matrix. In this process, heat is absorbed by the phenolic resin and is removed as the material ablates away. As a result, ablative TPS is heavy, often constituting up to 30% of a re-entry vehicle's mass, and is not reusable.

As a novel solution for these challenges encountering during atmospheric re-entry, the MHD (magnetohydrodynamic) Enhanced Entry System for Space Transportation (MEESST) project aims to manipulate plasma layer and heat flux of a vehicle using MHD effects. The MEESST project consists of a consortium of partner institutions, academic and industrial, each contributing specialist expertise in both numerical and experimental plasma dynamics. The consortium consists of academic institutions at; the Karlsruhe Institute of Technology (KIT), the University of Stuttgart's Institute of Space Systems (IRS), the University of Southampton, the Catholic University of Leuven (KU Leuven), the Von Karman Institute for Fluid Dynamics (VKI) and the University of Luxembourg. In addition, the consortium includes industrial institutions; Advanced Engineering Design Solutions (AEDS), THEVA, Neutron Star Systems and Absolut System.

MEESST's approach primarily relies on harnessing the Lorentz force to control the behaviour of the plasma enveloping the spacecraft, effectively minimizing thermal interaction between the harsh entry environment and the vehicle's surface materials[1]. Furthermore, the MEESST magnetic system exhibits the potential to offer supplementary advantages to space vehicles, including radiation shielding[2, 3]. This study encompasses the numerical investigations conducted by the University of Southampton and provides comparisons with experimental and numerical data generated by our consortium partners. The study aims to explore the effects of thermo-chemical non-equilibrium and MHD models for predicting radio blackout and heat flux manipulation.

2. Numerical Modelling

2.1. Governing Equations

The governing equations for the MEESST system are composed mainly of two parts, which are the flow field and the MHD field. The flow field equations describe a thermo-chemical non-equilibrium flow with MHD effects, Lorentz force and Joule heating. The governing equations of the flow field with the MHD effect, therefore, can be expressed in the following form:

$$\frac{\partial \mathbf{Q}}{\partial t} + \nabla \cdot (\mathbf{F} - \mathbf{F}_v) = \mathbf{S}_{NEQ} + \mathbf{S}_{MHD} \tag{1}$$

where $\mathbf{Q}$ is the vector of conservative variables, $\mathbf{F}$ is the inviscid flux vector, and $\mathbf{F}_v$ is the viscous flux vector, $\mathbf{S}_{NEQ}$ is the thermochemical non-equilibrium source terms and $\mathbf{S}_{MHD}$ is the source term related to MHD effects. The vector of conserved variables, $\mathbf{Q}$, is given by

$$\mathbf{Q} = \begin{Bmatrix} \rho_1 \\ \rho_2 \\ \vdots \\ \rho_s \\ \rho u \\ \rho v \\ \rho w \\ E \\ E_{ve} \\ E_e \end{Bmatrix} \tag{2}$$

where ρ_i is the density of species i, u, v and w are flow velocities, E is the total energy, E_{ve} is the vibrational-electronic energy, and E_e is the electron energy. The inviscid flux vector, $\mathbf{F}$, and viscous flux vector, $\mathbf{F}_v$, are expressed as:

$$\mathbf{F} = \begin{Bmatrix} \rho_1\mathbf{U} \\ \rho_2\mathbf{U} \\ \vdots \\ \rho_s\mathbf{U} \\ \rho u\mathbf{U} + \delta_{ij}p \\ \rho v\mathbf{U} + \delta_{ij}p \\ \rho w\mathbf{U} + \delta_{ij}p \\ (E+p)\mathbf{U} \\ E_{ve}\mathbf{U} \\ (E_e + p_e)\mathbf{U} \end{Bmatrix} \text{ and } \mathbf{F}_{v,i} = \begin{Bmatrix} -J_{i,1} \\ -J_{i,2} \\ \vdots \\ -J_{i,s} \\ \tau_{i,x} \\ \tau_{i,y} \\ \tau_{i,y} \\ \tau_{ij}\mathbf{U}_j - \left(q_{tr} + \sum_s^{All\ species} q_{ve,s} + q_e\right) - \sum(J_{i,s}h_s) \\ -\sum_s^{All\ species} q_{ve,s} \\ \tau_{ij,e}\mathbf{U}_j - q_{\boldsymbol{e}} - \left(J_{i,e}h_e\right) \end{Bmatrix} \tag{3}$$

where δ_{ij} denotes the Kronecker delta, $J_{i,s}$ is species diffusion flux in the i[th] direction, and τ_{ij} are components of the viscous stress tensor. q_{tr}, q_{ve} and $q_{\boldsymbol{e}}$ are translational-rotational, vibrational-electronic, and electron heat flux, respectively. The viscous stresses are modelled using Stokes' hypothesis under the assumption of a Newtonian fluid, and the heat fluxes for each energy mode are formulated according to Fourier's law. Modified Fick's law is employed to model the species mass diffusion fluxes whilst enforcing the sum of the diffusion fluxes equating to zero[4]. Wilke's semi-empirical mixing rule is utilised to model the mixture transport properties of viscosity, diffusion coefficients, and the thermal conductivity of each energy mode[5].

The thermochemical non-equilibrium source term, $\mathbf{S}_{NEQ}$, is described by

$$\mathbf{S_{NEQ}} = \begin{Bmatrix} \dot{\omega}_1 \\ \dot{\omega}_2 \\ \vdots \\ \dot{\omega}_s \\ 0 \\ 0 \\ 0 \\ 0 \\ S_{ve} \\ S_e \end{Bmatrix} \tag{4}$$

where $\dot{\omega}_s$ is the mass production rates of species s via chemical reactions, S_{ve} is the vibrational-electronics energy source term, and S_e is the electron energy source term. The vibrational-electronics energy source term, S_{ve}, can be described as:

$$S_{ve} = S_{ve-chem} + S_{ve-tr} + S_{vib-e} \tag{5}$$

where $S_{vib-chem}$ is the vibrational-electronic energy gained or removed by chemical reactions, S_{ve-tr} is the energy transferred between translational-rotational and vibrational-electronic modes, S_{vib-e} is the energy transfer between vibrational and electron energy modes. The radiation term indicating the rate of energy loss due to radiation caused by electronic transitions is not considered in this study for the simplification. The electron energy source term, S_e, can be described as[6]:

$$S_e = S_{e-chem} + S_{e-tr} + S_{e-vib} \tag{6}$$

where S_{e-chem} is the electron energy gained or removed by chemical reactions, S_{e-tr} is the energy transferred between translational-rotational and electron energy modes, S_{e-vib} is the energy transfer between vibrational and electron modes. In this study, the work done on electrons by the electric field induced by the electron pressure gradient, $-p_e\nabla\cdot\mathbf{U}$, is not considered.

The source term related to MHD effects, $\mathbf{S}_{MHD}$, can be expressed as:

$$\mathbf{S}_{MHD} = \begin{Bmatrix} 0 \\ 0 \\ \vdots \\ 0 \\ (\mathbf{J} \times \mathbf{B})_x \\ (\mathbf{J} \times \mathbf{B})_y \\ (\mathbf{J} \times \mathbf{B})_z \\ \mathbf{E} \cdot \mathbf{J} \\ \beta \frac{\mathrm{J} \cdot \mathrm{J}}{\sigma} \\ (1-\beta) \frac{\mathrm{J} \cdot \mathrm{J}}{\sigma} \end{Bmatrix} \tag{7}$$

where we assume the entire energy of the Joule heating goes into the vibration-electronic and electron energies modes, and β is the fraction of the Joule heating goes into the vibration-electronic mode and electron energy mode.The flow field equations, Eq. 1, are solved numerically using an in-house CFD code, which discretises physical systems according to the finite volume method upon a block-structured Cartesian mesh.

To include the MHD effect, we numerically solve the MHD equations which comes from Maxwell's equations with generalised Ohm's law as:

$$\nabla^2 \phi = \nabla \cdot (\mathbf{U} \times \mathbf{B}) \tag{8}$$

and

$$\mathbf{j} = \sigma(\mathbf{E} + \mathbf{U} \times \mathbf{B}) \tag{9}$$

where the Hall and ion-slip effects are neglected with low-magnetic Reynolds assumption. It is because the ion-slip effect does not have a considerable influence on the electric current, and the Hall effect does not have a negative influence on the MHD effects[7, 8]. The low magnetic Reynolds number assumption is quite reasonable because in the Newtonian limit, the typical magnetic Reynolds number is the order of 10^{-3} in a weakly ionised gas[9].

2.2. Simulation Geometry and Boundary Conditions

As part of a code verification and comparison study, an Argon flow system was chosen for numerical reproduction. This system simulated mirrors that of the experiments performed by Knapp et al.[10] with a magnetic probe immersed in an Argon plasma flow. The strength of the magnetic field issued by the probe was then varied, and the effect of this variation upon the plasma examined. The Knapp case experiments were originally conducted by IRS using their plasma wind tunnel PWK1, and showed a significant reduction in impinging heat loads when magnetic fields were applied. A schematic overview of the Knapp case's experimental setup, and the geometry of the magnetic probe used are shown in Fig. 1. The wall temperature is assumed to be 300K.

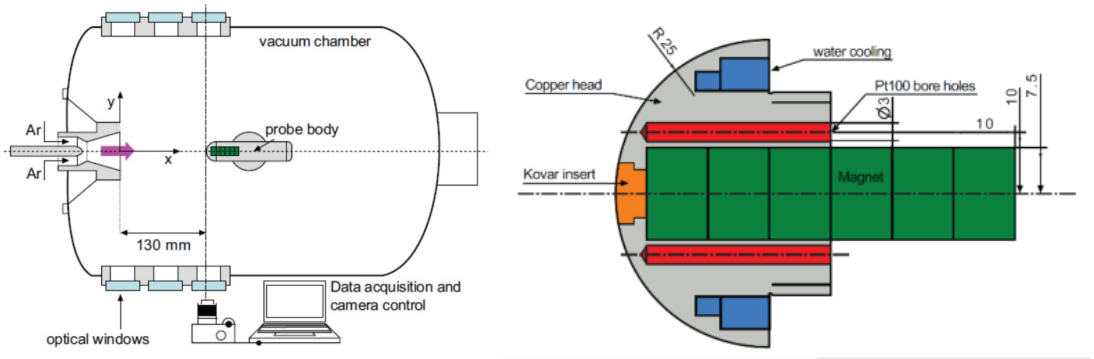

Figure 1. A schematic overview of the original Knapp experimental setup together with schematic of the magnetic probe utilised in Knapp's experiments. Images courtesy of IRS Stuttgart

Knapp's original experiments were performed with a variable magnetic probe to which small individual magnets were added to increase the magnetic field strength about the probe. This effect was simulated by manually aligning the magnetic field strength with the values used by Knapp. Simulations were performed with magnetic field strengths corresponding to zero, one and six magnets being present. The behavior of these magnetic fields across the simulation domain has been computed using the *magpylib* python library. The calculated magnetic field for 1-magnet and 6-magnet cases are shown in Fig. 2 and Fig. 3, respectively. The applied maximum magnetic field strength for 1-magnet and 6-magnet cases are 0.28T and 0.36T, respectively.

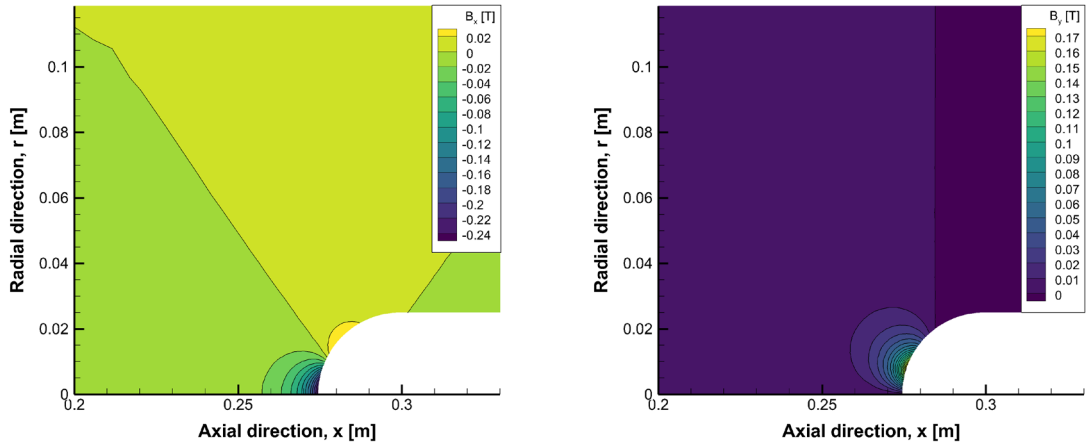

(a) (b)

Figure 2. Configuration of the applied magnetic field using magpylib python library for the 1 magnet case; (a) Azimuthal direction magnetic field. (b) Radial direction magnetic field

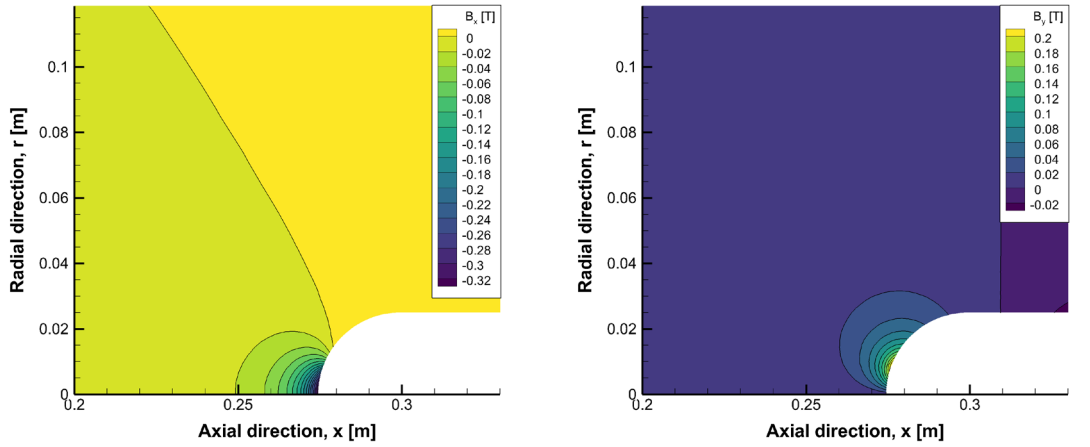

(a) (b)

Figure 3. Configuration of the applied magnetic field using *magpylib* python library for the 6 magnet case; (a) Azimuthal direction magnetic field. (b) Radial direction magnetic field

The measured plasma flow conditions for the Knapp's experiment are listed in Table 1[11], which were measured with intrusive techniques. These measured conditions are employed as inflow condition in this study with the 3 species argon model (Ar, Ar^+, and e^-). For the simplification, the wall temperature is assumed to be 300 K.

Table 1. Measured plasma flow conditions for Knapp's experiment [11].

Total pressure	240 ± 5 Pa
Heat flux	1263 ± 108 kW/m^2

Mass specific enthalpy	25.7 ± 4.6 MJ/kg
Electron temperature	17377 ± 2604 K
Electron density	$7.38 \pm 0.1 \times 10^{19}$ m^{-3}
Velocity	3100 m/s
Heavy particle temperature	8700 K
Ionisation degree	0.3

3. Results

3.1. In-house CFD code validation

The in-house non-equilibrium CFD solver, HANSA, is validated against several experimental and numerical results from the literature. In this section, we present the validation study performed against the LeMANS, which is a finite volume solver developed at the University of Michigan[15]. This problem involves hypersonic flow over a 2D cylinder with a diameter of 0.3048 m at two different Mach numbers, 10 and 25. The freestream conditions are taken from Lofthouse et al.[16], and nitrogen is considered as the gas species. The Knudsen number, based on the cylinder diameter, is 0.002, placing it in the slip regime where the continuum models are still applicable (at least for validation purposes) and the freestream temperature is set to 200 K for both cases. The wall temperature is fixed at 500 K and 1500 K for Mach 10 and 20 cases, respectively. We employ the Modified Steger-Warming (MSW) vector splitting approach to compute inviscid fluxes, except at the shock where the original S-W method is used, whereas viscous fluxes are computed using properties at the cell centres. A point implicit algorithm is applied for time integration.

The density, translational, and vibrational temperature flow contours predicted by the HANSA solver are compared with those from the LeMANS solver, as shown in Fig. 4. It is evident that the variations in flow properties predicted by HANSA closely align with the results obtained from LeMANS[15]. The translational and vibrational temperature variations along the stagnation streamline are also compared with LeMANS at Mach numbers 10 and 25, as shown in Fig. 5. The variation of properties including the shock standoff distance and peak temperature are in very good agreement with LeMANS, presented in Lofhouse et al [16].

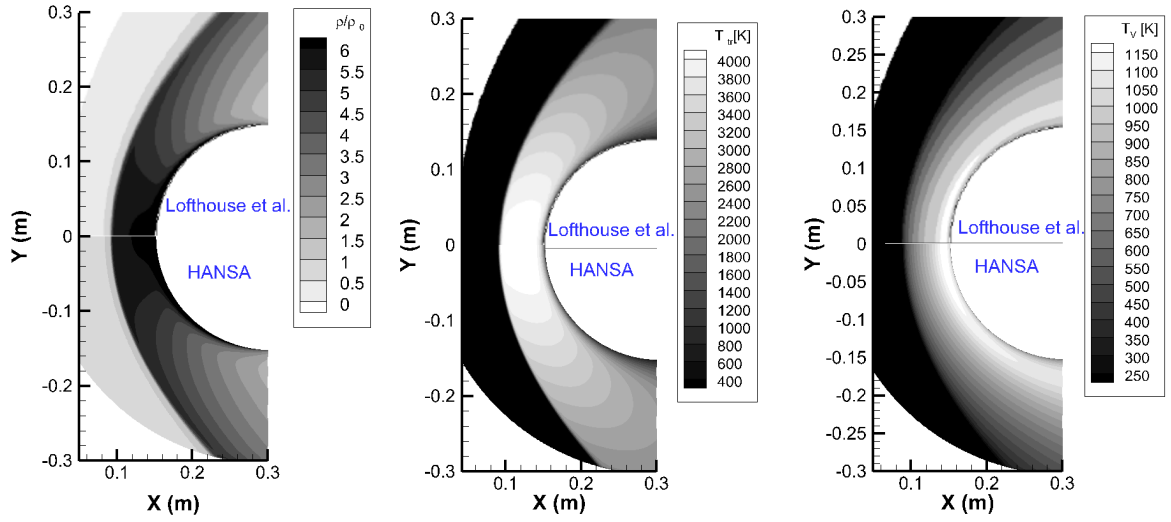

Figure 4. Flow contour of density ratio (normalised with freestream density), translation and vibrational temperatures obtained from HANSA (bottom) compared with LeMANS, presented in Lofthouse et al. (Top).

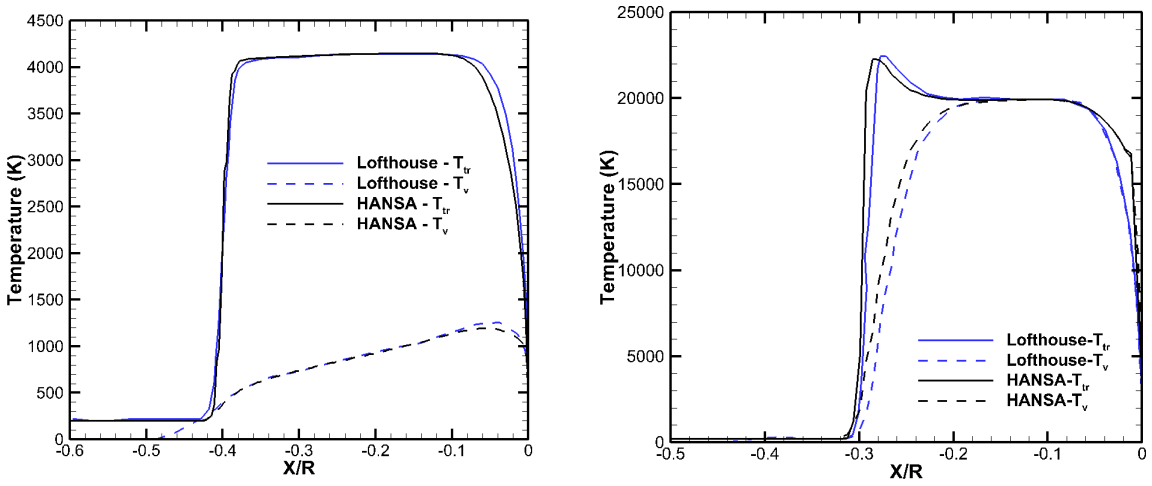

Figure 5. Comparison of translational and vibrational temperature variation along the stagnation streamline obtained from HANSA with LeMANS from Lofthouse et al.[13] The x-axis represents the negative distance from the stagnation point, normalised with the cylinder radius.

3.2. Schiaparelli capsule Martian atmospheric entry

Investigations of magnetic re-entry systems require the ability to reconstruct the behaviour of real capsules in atmospheric entry conditions. In this study, we have selected the ExoMars Schiaparelli capsule to validate the implemented thermos-chemical non-equilibrium models in the HANSA with considering the availability of real world data following its entry into Martian atmosphere[13,14]. Figure 4 shows the geometry of the Schiaparelli capsule which is a typical blunt body re-entry vehicle. The forebody shape of the Schiaparelli capsule is composed of a spherical nose with a 0.6 m radius, a cone, and a circular shoulder. The inflow conditions of the Schiaparelli capsule are listed in Table 3, which corresponds to the 56 km trajectory conditions. In this study, the freestream for the Martian atmosphere is assumed to be steady and laminar with the composition of 96% CO_2 and 4% N_2. The vehicle walls are assumed non-catalytic and iso-thermal, with a wall temperature of 1500K.

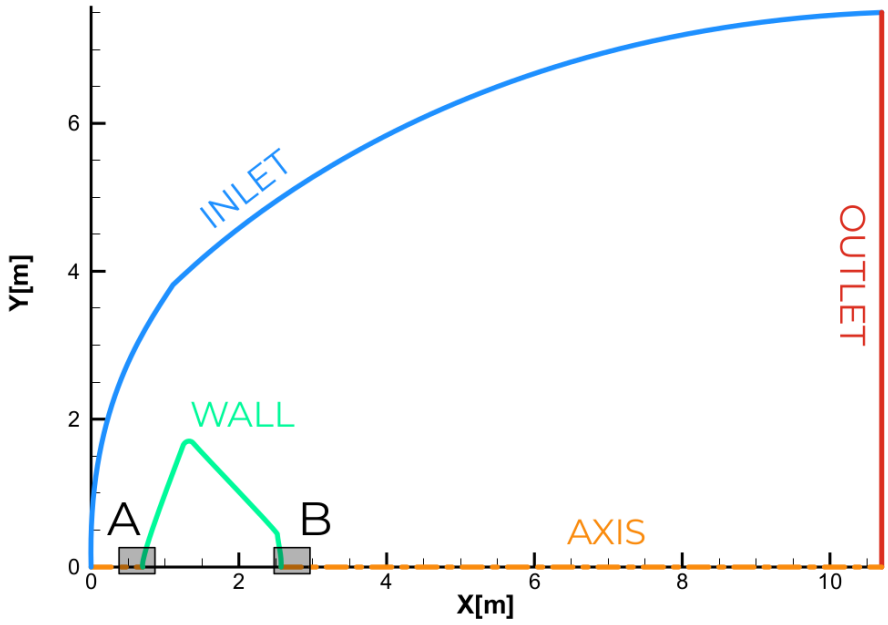

Figure 6. Simulation domain of the Schiaparelli capsule.

Table 2. Inflow conditions of the simulation which correspond to the 56 km altitude entry condition of the Schiaparelli capsule.

Inflow velocity, V_∞	$4516\ \mathrm{m/s}$
Freestream temperature, T_∞	$174\ \mathrm{K}$
Freestream density, ρ_∞	$5.82 \times 10^{-4}\ \mathrm{kg/m^{-3}}$
Freestream mole fraction	$\mathrm{X_{CO_2}} = 0.96; \mathrm{X_{N_2}} = 0.04$
Wall temperature, T_{wall}	$1500\ \mathrm{K}$

Figure 5 shows the simulated temperature contours. As can be seen, the simulated flow field using HANSA shows the formation of a Mach disk at the core of the wake. A similar phenomenon has previously been observed by Wright et al.[14] for the Phoenix aeroshell during Mars entry. As shown in Figure 6, the vast majority of electrons in the flow are present in the bow shock and the post-shock region. The electron number density in the wake region can also been seen to be lower than the critical number density for a communication blackout.

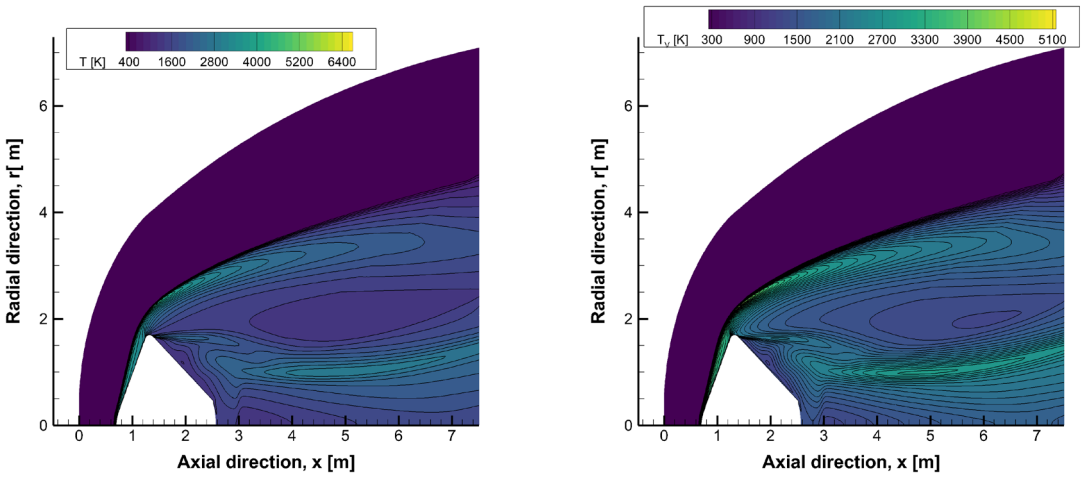

(a) (b)

Figure 7. Temperature contour of the Schiaparelli capsule at 56 km entry condition; (a) Translational-rotational temperature. (b) Vibrational-electronic temperature.

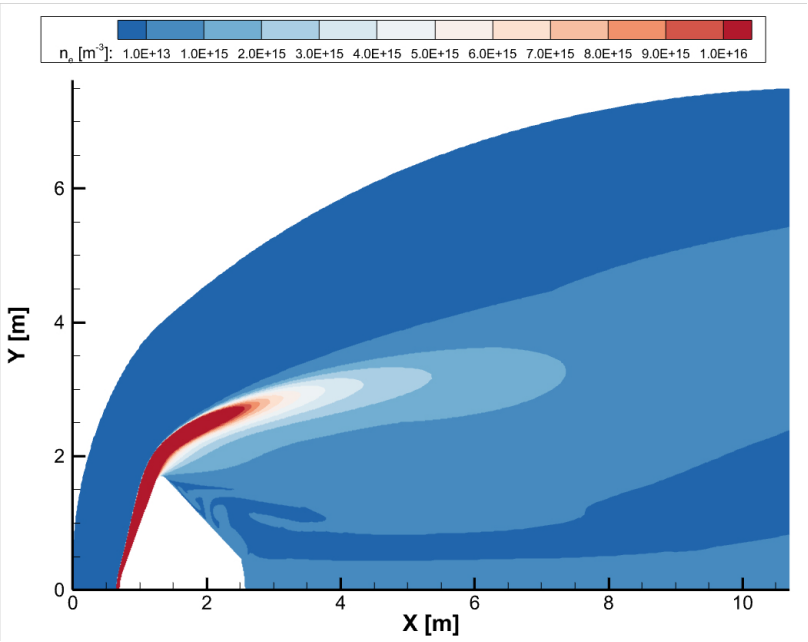

Figure 8. Electron number density of the Schiaparelli capsule at 56 km entry condition.

3.3. MHD effects

Figure 7 and Figure 8, respectively, heavy particle temperature and electron temperature contours near the Knapp's probe with and without the magnetic field. As can be seen, the location of the shock is shifted due to the MHD effects, the Lorentz force, which is induced by the applied magnetic field. A stronger magnetic field, therefore, shows larger enhancement of the shock standoff distance.

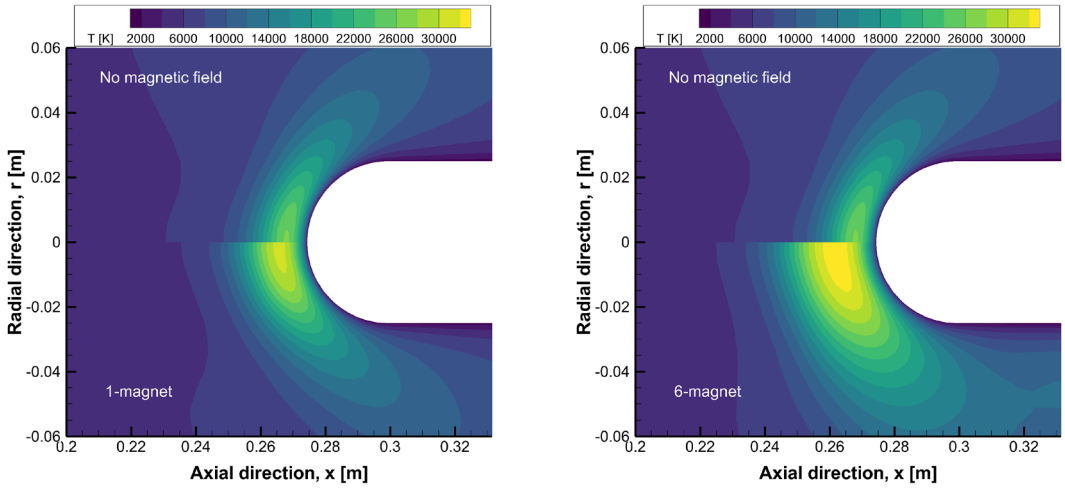

(a) (b)

Figure 9. Heavy particle temperature fields, T, proximate to the probe nose for 1 and 6 magnets compared with the 0 magnet case. (a) 1-magnet case. (b) 6-magnet case.

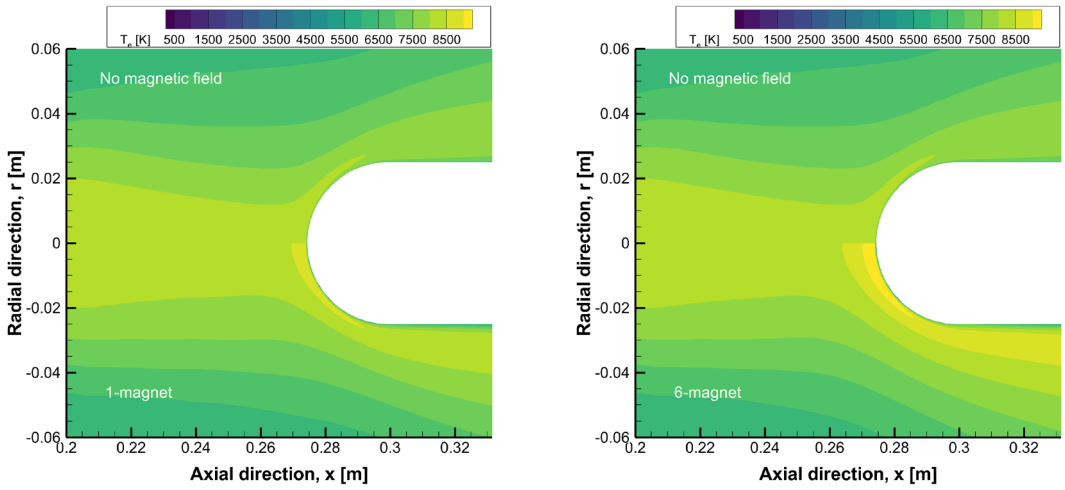

(a) (b)

Figure 10. Electron temperature fields, T_e, proximate to the probe nose for 1 and 6 magnets compared with the 0 magnet case. (a) 1-magnet case. (b) 6-magnet case.

Table 3 compares the peak heat flux with and without a magnetic field, alongside experimental data from Knapp's study [11]. As can be observed, the model accurately predicts the heat flux measured in the experiment when no magnetic field is applied. However, when a magnetic field is introduced, the model predicts a reduction in peak heat flux of 10% and 16% for the 1-magnet and 6-magnet configurations, respectively.

Table 3. Comparison of peak stagnation heat flux against the experimental results from Knapp's study[11].

	No magnetic field	1-magnet case	6-magnet case
Experiment[11]	$1235.38 \pm 200 \mathrm{kW/m^2}$	·	·
Simulation	$1407.7\ \mathrm{kW/m^2}$	$1274.9\ \mathrm{kW/m^2}$	$1182.1\ \mathrm{kW/m^2}$

4. Conclusion

In this study, we have presented a series of simulations conducted using the University of Southampton's HANSA Computational Fluid Dynamics (CFD) toolkit as the framework of the Magnetic Enhanced Entry Systems for Space Transportation (MEESST) project. The MEESST project aims to pioneer innovative magnetic plasma control methods for spacecraft re-entry. A concise overview of the methodology employed by HANSA is furnished to offer context and promote the reproducibility of the ensuing outcomes. The simulations are contextualized within the broader scope of the MEESST project, with concurrent experimental endeavors by MEESST collaborators being outlined. The outcomes encompass simulations illustrating heat flux manipulation using MHD effects, along with comprehensive capsule simulations.

The three showcased simulation campaigns herein underscore HANSA's proficiency in contributing to the advancement of magnetic plasma control systems and its capability simulating thermos-chemical nonequilibrium flows A code-to-code comparison of HANSA against LeMANS showcases the accuracy of the thermo-chemical non-equilibrium models implemented in HANSA. The results from the Knapp case illustrate the effective manipulation of Argon plasma under magnetic influence. Likewise, the Schiaparelli simulations underscore HANSA's capacity to simulate entire capsules, encompassing intricate thermochemical interactions, within a Martian atmosphere. These endeavors underscore the ability of MEESST collaborators to consistently simulate systems pertinent to magnetic plasma manipulation aboard re-entry spacecraft.

This capability will be further leveraged in the remaining phases of the MEESST project to compile a comprehensive dataset showcasing the effects of magnetic plasma manipulation. This dataset will facilitate comparisons with previous studies utilizing Argon plasma, providing insights into the influence of plasma composition on magnetic responsiveness. Such research avenues hold promise for future investigations utilizing Martian atmosphere plasma, potentially offering valuable insights for missions within the Artemis program and beyond.

Acknowledgements

The authors would like to thank the other members of the MEESST consortium for the key work that they've undertaken. Without their contributions, the work within this paper would not have been possible. This work was made possible by the Future and Emerging Technologies (FET) programme within the European Commission's Horizon 2020 scheme [grant no. 899298] The authors would also like to acknowledge use of the IRIDIS high performance compute cluster at the University of Southampton and offer their thanks to the IRIDIS team.

References

[1] A. Lani, et al., "A Magnetohydrodynamic enhanced entry system for space transportation: MEESST," *Journal of Space Safety Engineering*, **10** (1), 2023

[2] P. Desiati and E. D'Onghia. Crew hat: A magnetic shielding system for space habitats, 2022.

[3] K. Ferrone, C. Willis, F. Guan, J. Ma, L. Peterson, and S. Kry, "A review of magnetic shielding technology for space radiation," *Radiation*, **3**(1):46–57, 2023

[4] K. Shutton and P. A. Gnoffo, "Multi-component diffusion with application to computational aerothermodynamics," AIAA Paper 1998-2575, 1998

[5] C. R. Wilke, "A viscosity equation for gas mixtures," *Journal of Chemical Physics*, **18**:517–519, 1950

[6] M. Kim and I. D. Boyd, "Effectiveness of a Magnetohydrodynamics system for Mars entry," *Journal of Spacecraft and Rockets*, **49**(6), 2012

[7] T. Fujino, H. Sugita, M. Mizuno, I. Funak, and M. Ishikawa, "Influences of Electrical Conductivity of Wall on Magnetohydrodynamic Control of Aerodynamic Heating," *Journal of Spacecraft and Rockets*, **43**(1), 2006

[8] T. Fujino, I. Funak, I., M. Mizuno, H. Sugita, and M. Ishikawa, "Developing Field Emitter Array Cathode Systems for Electrodynamic Tether Propulsion," AIAA Paper 2004-2561, 2004

[9] J.S. Shang, J. Menart, J., R. L. Kimmel, and J. Hayes, "Hypersonic Inlet with Plasma Induced Compression," AFRL-VA-WP-TP-2006-333, Jan 2006.

[10] A. Knapp et al, "Investigation of mhd impact on argon plasma flows by variation of magnetic flux density," *Open Plasma Physics Journal*, **5**(1), 2012.

[11] A. Knapp, Experimentelle Untersuchung von magnetohydrodynamischen Einflüssen auf Plasmaströmungen, PhD thesis, Institut für Raumfahrtsysteme, Universität Stuttgart, 2012.

[12] Andrew Ball, Thierry Blancquaert, Olivier Bayle, Leila Lorenzoni, and A. Haldemann, "The exomars Schiaparelli entry, descent and landing demonstrator module (edm) system design," *Space Science Reviews*, **218**, 08 2022.

[13] D. Bonetti, G. De Zaiacomo, G. Blanco, I. P. Fuentes, S. Portigliotti, O. Bayle, and L. Lorenzoni, "Exomars 2016: Schiaparelli coasting, entry and descent post flight mission analysis," *Acta Astronautica*, **149**:93–105, 2018

[14] M. J. Wright, C. Y. Tang, K. T. Edquist, B. R. Hollis, P. Krasa, and C. A. Campbell, "A review of aerothermal modeling for mars entry missions," 48th AIAA Aerospace Sciences Meeting Including the New Horizons Forum and Aerospace Exposition, 2010.

[15] L. C. Scalabrin, L. C. (2007). Numerical simulation of weakly ionized hypersonic flow over reentry capsules, PhD thesis, University of Michigan, 2007

[16] A. J. Lofthouse Nonequilibrium Hypersonic Aerothermodynamics Using the Direct Simulation Monte Carlo and Navier-Stokes Models, PhD thesis, University of Michigan, 2008